

Similarity Spectra and Coherence-Based Analysis of Noise
from an Installed GE-F404 Engine

Kristi A. Epps

A senior thesis submitted to the faculty of
Brigham Young University
in partial fulfillment of the requirements for the degree of

Bachelor of Science

Kent L. Gee, Advisor

Department of Physics and Astronomy

Brigham Young University

Copyright © 2023 Kristi A. Epps

All Rights Reserved

ABSTRACT

Similarity Spectra and Coherence-Based Analysis of Noise from an Installed GE-F404 Engine

Kristi A. Epps

Department of Physics and Astronomy, BYU

Bachelor of Science

Because the noise source mechanisms and radiation properties associated with high-thrust, tactical jet engines are not fully understood, analysis of full-scale measurements are conducted to improve the understanding of these characteristics. Two such analyses used in this thesis are: 1) compare spectral data to empirical models for jet noise spectra, and 2) calculate the coherence between microphones for varying frequencies. This paper compares measured near-field spectra from a T-7A-installed GE F404-103 engine with analytical similarity spectra for fine-scale mixing noise, large-scale mixing noise, and broadband shock-associated noise. It also compares the coherence to narrowband autospectral density levels at specified frequencies. The similarity spectra and coherence analyses enable the determination of spatial trends in overall sound pressure level, peak frequency, and spatio-spectral lobes. They also help determine the relative importance of each type of noise radiation as a function of location. This approach is used to gain insights on spatial and frequency trends for different engine conditions. Additionally, it is used for rapid comparisons to analyses of other aircraft and jets of other scales and conditions.

Keywords: broadband shock-associated noise, coherence, F404 engine, full-scale, high-performance aircraft, jet noise, Mach wave radiation, near-field, similarity spectra, spatio-spectral lobes

ACKNOWLEDGMENTS

The similarity spectra analysis discussed in this thesis was funded under Air Force Research Laboratory Case No. 88ABW-2020-3238 and under Office of Naval Research Grant No. N00014-21-1-2069, DCN #43-8908-21. The results from that research were presented at the 179th and 181st Meetings of the Acoustical Society of America in 2020 and 2021. The coherence analysis was funded under Office of Naval Research Grant No. N00014-21-1-2069, the results of which were presented at the 183rd Meeting of the Acoustical Society of America in 2022. All research shown in this thesis has also been supported by mentored research funds from Brigham Young University. Measurements were funded by the Air Force Research Laboratory. The Advanced Pilot Training Systems Program Office and Holloman Air Force Base are thanked for their cooperation in carrying out this study. I would like to thank my advisor, Dr. Kent Gee, for his guidance on this research as well as his support in my efforts to achieve my goals. I couldn't have found my direction without you. I would also like to thank Kevin Leete and Aaron Vaughn for teaching me how to do jet noise research, and my fellow research students Logan Mathews, Matthew Christian, Tyce Olaveson, and Cooper Merrill for their assistance and the many jokes they can't seem to stop sharing. Thanks to you, I will never be able to forget that jets are loud. Last of all, I would like to thank my family for their constant encouragement and support. If you don't understand anything else in this thesis, understand that I love you and will be forever grateful for you. Team Epps all the way!

Contents

| | |
|--|------------|
| Table of Contents | vii |
| List of Figures | ix |
| 1 Introduction | 1 |
| 1.1 Overview | 1 |
| 1.2 A Review of Jet Noise | 2 |
| 1.3 The Components of Jet Noise | 3 |
| 1.4 The Similarity Spectra Analysis | 4 |
| 1.5 The Coherence Analysis | 6 |
| 1.6 The T-7A Red Hawk | 8 |
| 2 Methods | 9 |
| 2.1 Overview | 9 |
| 2.2 Conditions of the Measurement Environment | 9 |
| 2.3 Measurement Procedures | 11 |
| 2.4 Microphone Array Setup | 11 |
| 2.5 Encountering Non-Acoustic Sources of Noise | 14 |
| 3 Results | 15 |
| 3.1 Overview | 15 |
| 3.2 Applying the Similarity Spectra Analysis | 15 |
| 3.2.1 At 88% N2 | 16 |
| 3.2.2 At Afterburner | 20 |
| 3.3 Applying the Coherence Analysis | 24 |
| 3.3.1 At 88% N2 | 24 |
| 3.3.2 At Afterburner | 26 |
| 3.4 Decomposing the Spatiospectral Lobes | 28 |
| 3.5 Conclusion | 30 |
| Bibliography | 35 |

Index

41

List of Figures

| | | |
|-----|---|----|
| 1.1 | Diagram of the components of jet noise | 4 |
| 1.2 | The similarity spectra models | 5 |
| 1.3 | Example of a coherence plot | 7 |
| 1.4 | Image of the T-7A Red Hawk | 8 |
| 2.1 | T-7A facing the jet blast deflector | 10 |
| 2.2 | Images of microphones in the near-field ground array | 12 |
| 2.3 | Diagram of the microphone locations in the near-field ground array | 13 |
| 3.1 | Similarity spectra fits for 88% N2 at upstream and sideline angles | 17 |
| 3.2 | Similarity spectra fits for 88% N2 at downstream angles | 19 |
| 3.3 | Similarity spectra fits for afterburner at upstream and sideline angles | 21 |
| 3.4 | Similarity spectra fits for afterburner at downstream angles | 23 |
| 3.5 | Coherence maps for 88% N2 at 98, 266, 470, and 698 Hz | 25 |
| 3.6 | Coherence maps for afterburner at 98, 266, 470, and 698 Hz | 27 |
| 3.7 | Evidence of spatio-spectral lobes in a similarity spectra fit, coherence map, and spatio-spectral map | 29 |

Chapter 1

Introduction

1.1 Overview

This section introduces the concept of jet noise, how it is generated, and how it can be analyzed. Sec. 1.2 discusses the contribution of jet noise to hearing loss and current methods used to minimize it. Sec. 1.3 reviews the different sources of jet noise and how each propagates. The next two sections introduce two analyses that identify and characterize jet noise sources. Sec. 1.4 describes the similarity spectra analysis, which compares the sound pressure level between measured spectra and calculated spectral models to characterize source behavior. Sec. 1.5 discusses the coherence analysis, which compares the time signals between two microphones to determine their similarity, or coherence. Because each source of jet noise has different coherence properties, their spatial and frequency trends can be identified. Sec. 1.6 introduces the T-7A Red Hawk, a new trainer aircraft for the US Air Force. Measurements were taken of the T-7A aircraft and similarity spectra and coherence analyses were applied to the resultant data. The results of these analyses are shown in Sec. 3.2 and Sec. 3.3.

1.2 A Review of Jet Noise

One of the main goals of all jet noise research is to reduce the amount of noise experienced by military personnel and nearby communities without affecting the performance of the aircraft. Whether the aircraft cruises at a lower power or needs to launch off an aircraft carrier with enough speed to stay aloft, the noise generated by military aircraft can reach levels that are damaging to human hearing within minutes, or even seconds, of being exposed to them. While hearing protection provides a necessary and helpful barrier to this noise, military personnel still experience significant hearing loss [1] that cannot be regained. By reducing the noise an aircraft generates, those who work near operating aircraft can be assured of a greater likelihood of preserving their hearing.

There are many different varieties of aircraft noise that can be and have been greatly reduced. Engines, fans, compressors, and other mechanical parts are designed to operate more efficiently and quietly than their predecessors. Jet noise, however, is produced through the physical processes of fluid dynamics. When the exhaust from the aircraft exits the nozzle and mixes with the air around it, the air becomes turbulent and generates noise. The roaring sound mixed with some crackling that comes from a fighter jet soaring over the football stadium is the product of this turbulence.

Some methods have already been identified and implemented to reduce the jet noise military aircraft generate [2–5]. Most of these noise reduction technologies, however, involve breaking up the flow from the exhaust. While this effectively reduces the jet noise, it also reduces the thrust an aircraft produces and thus affects its performance capabilities. Because jet noise is generated by a physical process that also allows the aircraft to perform properly, it is harder to determine its sources and how to reduce the noise without affecting the performance of the aircraft. Through identification and characterization of these sources it will become possible to determine the best method of noise reduction.

1.3 The Components of Jet Noise

As was mentioned previously, jet noise is generated when the turbulent exhaust of a jet engine mixes with the ambient air, creating acoustic waves that, to some degree, radiate in all directions. For a supersonic jet exhaust from a full-scale, installed engine, three main types of turbulence-induced noise [6, 7] are believed to dominate, although other sources are being investigated [8]. Turbulent mixing noise consists of large-scale noise (LSN) radiated from large-scale, coherent structures and fine-scale noise (FSN) radiated from fine-scale turbulence. Additionally, interaction of the large-scale turbulent structures with shock cells generates broadband shock-associated noise (BSN). These shock cells only appear at higher engine powers, so BSN will only be observed at higher engine powers. Screech, a feedback-amplified tonal noise generated at the shock cells, has been studied at the laboratory-scale [9, 10] but does not factor significantly in actual high-performance jet engine exhausts.

Figure 1.1 shows a diagram of the jet, the three types of turbulent structures, and their primary radiation characteristics. FSN is relatively spatially incoherent, and thus radiates in all directions. It tends to dominate upstream (to the front of the aircraft, also called the forward direction) and to the sideline. On the other hand, LSN dominates at downstream angles (behind the aircraft, also called the aft direction). When present, BSN preferentially radiates upstream and tends to be visible in spectra at angles that are dominated by FSN, but it has a narrower bandwidth than FSN and a greater peak frequency that increases with increasing inlet angle. Knowing these source and radiation characteristics, analyses that focus on spatial and frequency trends can be used to find additional insight into their behavior.

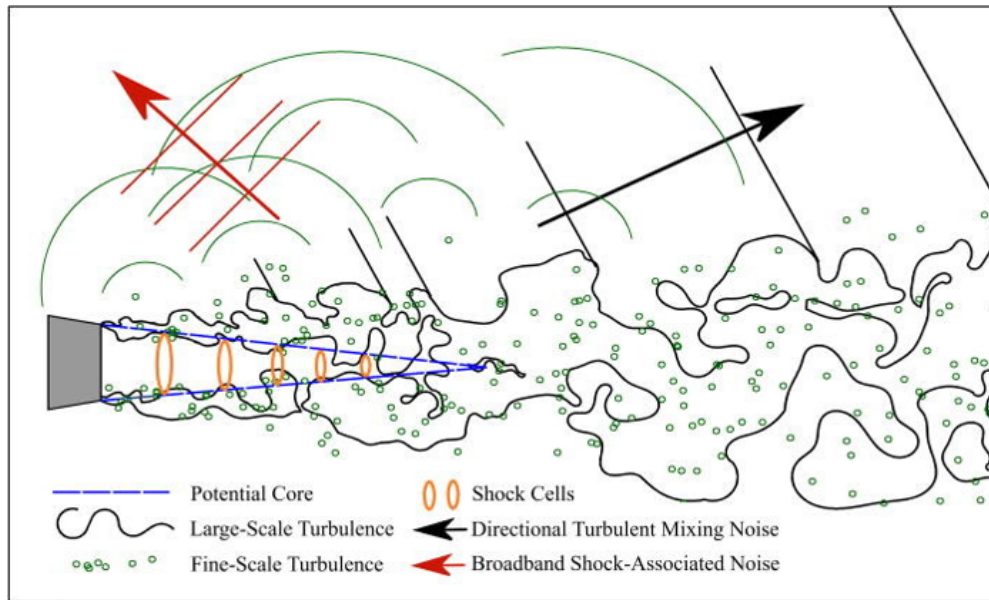


Figure 1.1 Diagram of jet noise and different source characteristics, copied from Vaughn *et al.* [11]

1.4 The Similarity Spectra Analysis

Building on an assumption that both fine- and large-scale turbulence contribute to the noise radiation from a jet, and that their spectral characteristics were likely different, Tam *et al.* [12] used several laboratory-scale datasets to develop a fine-scale similarity spectrum model $L_F(f)$ and a large-scale similarity spectrum model $L_L(f)$. The $L_F(f)$ spectrum has a broad peak and round spectral shape, whereas the $L_L(f)$ spectrum has a narrower peak (see Fig. 1.2) with power-law roll-up and roll-off that corresponds to greater temporal correlation [13]. Tam *et al.* compared these similarity spectra to the measured spectra $L_p(f)$ (represented as a power spectral density) to determine where the different turbulent structures appear. While these models were originally used to fit far-field laboratory-scale data, Neilsen *et al.* [14] found that they could also be used to reasonably fit near-field data from a high-performance, afterburner-capable tactical aircraft. Other full-scale similarity spectra analyses have been conducted [8, 14–16] and have even been used to create level-based wavepacket models [17].

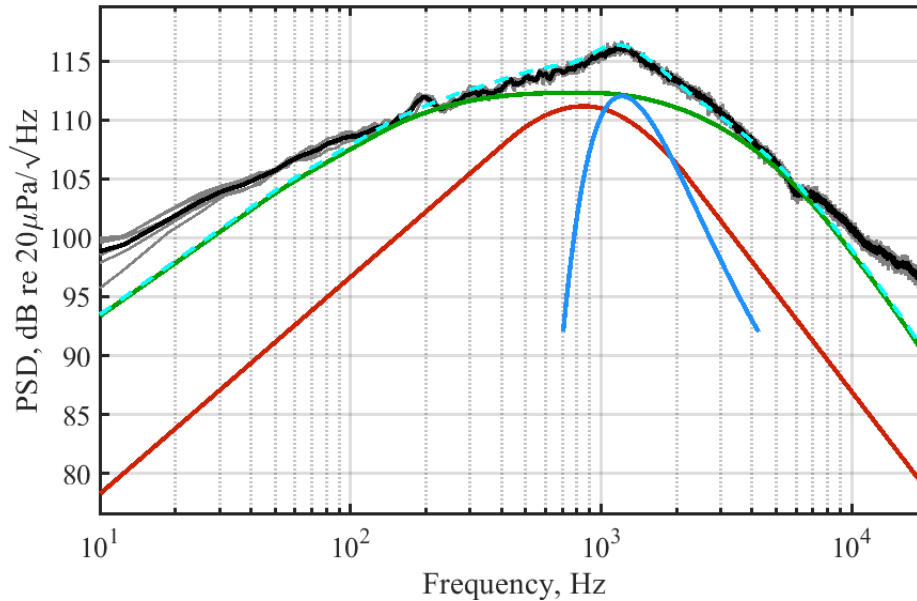


Figure 1.2 Application of the similarity spectra using a measured spectrum from the T-7A data. The large-scale similarity spectrum $L_L(f)$ (red curve), fine-scale similarity spectrum $L_F(f)$ (green curve), and BSN model $L_B(f)$ (blue curve) can be added together to create a combined model $L_T(f)$ that is used to fit the measured spectrum. The gray lines indicate the spectra of individual runs (see Sec. 2.3) and the black line indicates an average of those runs ($L_p(f)$). The similarity spectra are fitted to the average curve.

Although not adopted nearly as extensively as Tam *et al.*'s $L_F(f)$ and $L_L(f)$, empirically derived, analytical models for BSN spectral shapes can also be incorporated into a similarity spectra analysis. This was done for noise from the F-35B by Neilsen *et al.* [15] using the model for BSN $L_B(f)$ created by Kuo *et al.* [7] Whereas the $L_F(f)$ and the $L_L(f)$ spectra have only two adjustable parameters – peak frequency and level – the $L_B(f)$ spectrum has an additional parameter that adjusts the spectral width. In order to eventually compare fits for different aircraft in different studies, the same fitting functions are used in the current analysis.

Tam *et al.* [16] also produced a model spectrum for BSN and similarly noted the need for three adjustable parameters for a BSN spectral model, but their model was not used in conjunction with their other similarity spectra. By comparing $L_F(f)$, $L_L(f)$, and $L_B(f)$ to the measured spectra, it is possible to determine the sources of jet noise that contribute to the total measured spectrum at

different observer locations. It is noted that fitting the $L_F(f)$, $L_L(f)$, and $L_B(f)$ spectra to the $L_p(f)$ data is done manually and usually collaboratively. Once fits have been made, they are presented to the research advisor and other jet noise research students to determine if they could be improved. This collaborative effort is repeated until the best fits possible are determined and produced. It is also an iterative process, meaning that trends in fitting parameters and in resulting levels are expected to vary relatively smoothly.

It is noted that previous studies using Tam *et al.*'s similarity spectra have used nomenclature inconsistently (such as "FSS" and "LSS"), resulting in confusion about whether the label was referring to mixing noise phenomena or the empirical spectral curves. This thesis attempts to distinguish the mixing noise phenomena from the models used to identify their spectral characteristics by using a new nomenclature first defined in Epps *et al.* [18] that clarifies which phenomenon or model is being referenced.

1.5 The Coherence Analysis

Finding the coherence between two microphones is another method of characterizing the radiation of jet noise sources. Mathematically, coherence is defined as

$$\gamma_{xy}^2(f) = \frac{|G_{xy}(f)|^2}{G_{xx}(f)G_{yy}(f)}, \quad (1.1)$$

where G_{xy} is the cross-spectrum of two microphone signals $x(t)$ and $y(t)$, G_{xx} is the autospectrum of signal $x(t)$, G_{yy} is the autospectrum of signal $y(t)$, and f is the frequency. The cross-spectral measurement is divided by the autospectra to normalize it, resulting in bounded coherence values between 0 and 1. Physically, coherence indicates how similar two signals are by comparing the information they contain at specific frequencies.

Figure 1.3 is an example of a coherence plot. A comparison between microphones at 40° and 100° , for example, reveals that there is little to no coherence, and thus little to no similarity, between

the signals received at these two different locations. A comparison between microphones at 120° and 140° , however, indicates that there is a higher level of coherence, and thus greater similarity, between the signals at these two locations. The diagonal between the bottom left and top right corners shows a coherence of 1, which is expected because the comparison is between the same signal at one location, and one signal is always self-similar.

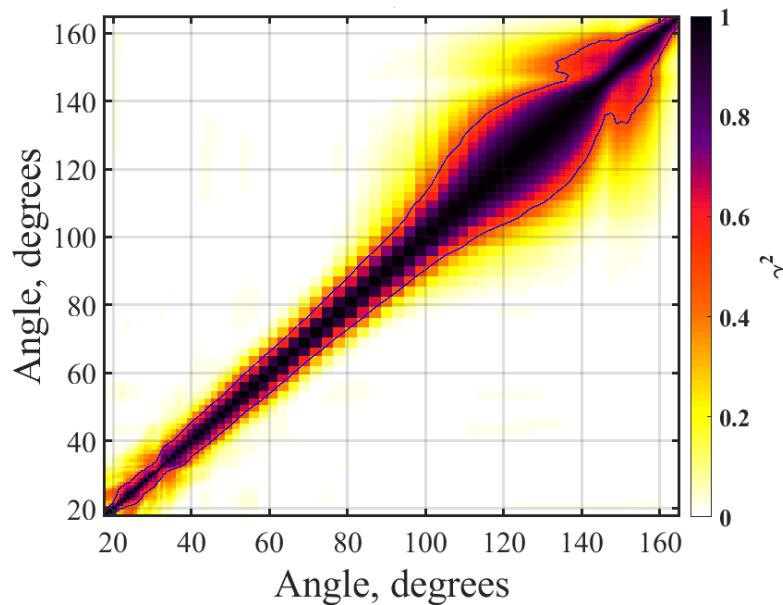


Figure 1.3 A typical coherence plot. Comparing the level of coherence between two microphone locations indicates how similar the two signals received at those locations are.

Each of the three main noise components, FSN, LSN, and BSN, has unique coherence properties. FSN is known to be largely incoherent due to its random radiating behavior, so at locations where FSN tends to dominate the coherence can be expected to drop significantly. This typically occurs at sideline locations. LSN is known to be much more coherent than FSN, so the coherence is expected to increase at locations farther downstream of the aircraft where the radiated waves from LSN tend to dominate. BSN is also largely coherent, so the coherence can be expected to increase between upstream locations where BSN tends to dominate. Because BSN is only generated at higher engine powers (see Sec. 1.3), coherence between upstream locations will be greater at those engine powers.

Harker *et al.* [19], Swift *et al.* [20], and Leete *et al.* [21] have identified these noise characteristics in their studies.

1.6 The T-7A Red Hawk

A few different military aircraft have been studied in a full-scale environment by the jet noise students at Brigham Young University. The most recent aircraft studied is the T-7A Red Hawk. This aircraft (see Fig. 1.4) is a new high-performance trainer aircraft developed for the United States Air Force by Boeing. It has a single GE F404-103 engine that can produce about 11,000 kN (lbf) of thrust without afterburner and 17,000 kN (lbf) with afterburner. Variants of the F404 appear in single- (KAI/LMTAS T-50) and twin-engine (F/A-18 C/D) tactical aircraft [22] and its noise reduction has been studied by others [2–5]. Its derivative, the F414 engine, powers the F/A-18 E/F Super Hornet. Studying the noise radiation from the T-7A can help identify differences between single- and twin-engine configurations and aid in further noise reduction efforts. BYU students were given the opportunity to take measurements on a T-7A aircraft in the summer of 2019. They used specialized equipment and microphone arrays to optimize the data required for various analyses. A description of the methods used to conduct these measurements is discussed in Chapter 2.



Figure 1.4 An image of the T-7A Red Hawk. Photo copied from the DVIDS website: <https://www.dvidshub.net/image/5754020/asecaf-announces-t-7a-red-hawk-during-air-space-and-cyber-conference>

Chapter 2

Methods

2.1 Overview

This section reviews the procedures and equipment involved in the data collection of jet noise of a T-7A aircraft. Measurements were taken in a full-scale environment at Holloman Air Force Base (Sec. 2.2) in the summer of 2019. The details of how the measurements were performed are given in Sec. 2.3. Over 200 microphones were used in various arrays, which ranged from distances very near the aircraft to nearly 230 m (755 ft) away. This thesis only analyzes the results of 120 microphones set up in a near-field ground array; details on this array of microphones are in Sec. 2.4. Some non-acoustic noise sources were observed in the unprocessed data, and efforts were made to reduce that noise as outlined in Sec. 2.5.

2.2 Conditions of the Measurement Environment

Measurements of the T-7A aircraft were planned and executed to maximize the validity and significance of the data. These measurements were taken on 18 August 2019 at Holloman Air Force Base in New Mexico. They are described in detail by Leete *et al.* [23], but relevant details are



Figure 2.1 Picture of the T-7A aircraft on the run-up pad facing the jet blast deflector. Some mounted microphone arrays can be seen in the foreground. Photo taken by a member of BYU's jet noise research group.

repeated here.

For these measurements, the aircraft was uniquely positioned to allow for an analysis of the noise at locations very far downstream. As seen in Fig. 2.1, the T-7A was tied down to a concrete run-up pad with the nose pointing towards the jet blast deflector. A jet blast deflector is meant to redirect the flow of exhaust from an aircraft away from the tarmac to prevent any damage or injury to equipment or personnel, so the aircraft is typically placed with the exhaust flowing towards the deflector. For these measurements, however, the T-7A was intentionally positioned with the exhaust flowing down the run-up pad to create an undeflected plume environment.

Many environmental factors can contribute to different phenomena observed in the raw data, so efforts must be taken to record these factors for future use in data validation and analysis. The measurements were taken between 5 AM and 7 AM local time to avoid prevailing winds and limit their effect on the data. Weather stations were set up to record ambient temperature, pressure, humidity, and wind speed and direction during the measurements. While recording, the temperature ranged from 19.9-25.8 °C, the humidity from 21.9-31.9%, and the average wind speed was 1.9 kts.

The terrain in the immediate vicinity of the pad was mostly comprised of dirt and was relatively flat. At distances farther afield, however, the terrain became more uneven and overgrown with brush, which sometimes matched the height of mounted microphones.

2.3 Measurement Procedures

The engine was cycled through multiple engine powers multiple times to decrease the likelihood that factors from the environment or equipment would make the data unusable. These engine conditions included 82% N2, 88% N2, military power (maximum thrust dry), and afterburner (maximum thrust wet). The military power and afterburner engine conditions will subsequently be referred to as MIL and AB, respectively.

An ambient measurement was taken prior to the engine startup. The Auxiliary Power Unit (APU) startup sequence was then run and completed before the engine was started and run at idle. The engine was then run at 75% N2, 82% N2, 88% N2, MIL, and AB with each engine condition running long enough for the data acquisition systems to record for thirty seconds before moving on to the next power level. After running at AB, the engine was brought down to idle for a few minutes to cool down before it was run through the same sequence again. Once the engine had finished running at AB for the second time, the engine was powered down. This whole process was repeated two more times, resulting in a total of six runups (or runs) at each condition. In this analysis, results of only the 88% N2 and AB engine conditions are shown.

2.4 Microphone Array Setup

Although a larger number of microphones were part of the measurement, only the results from microphones along a 120-microphone near-field ground array (also referred to as the Imaging array) are analyzed. The array was located on the left side of the aircraft, but subsequent diagrams of the

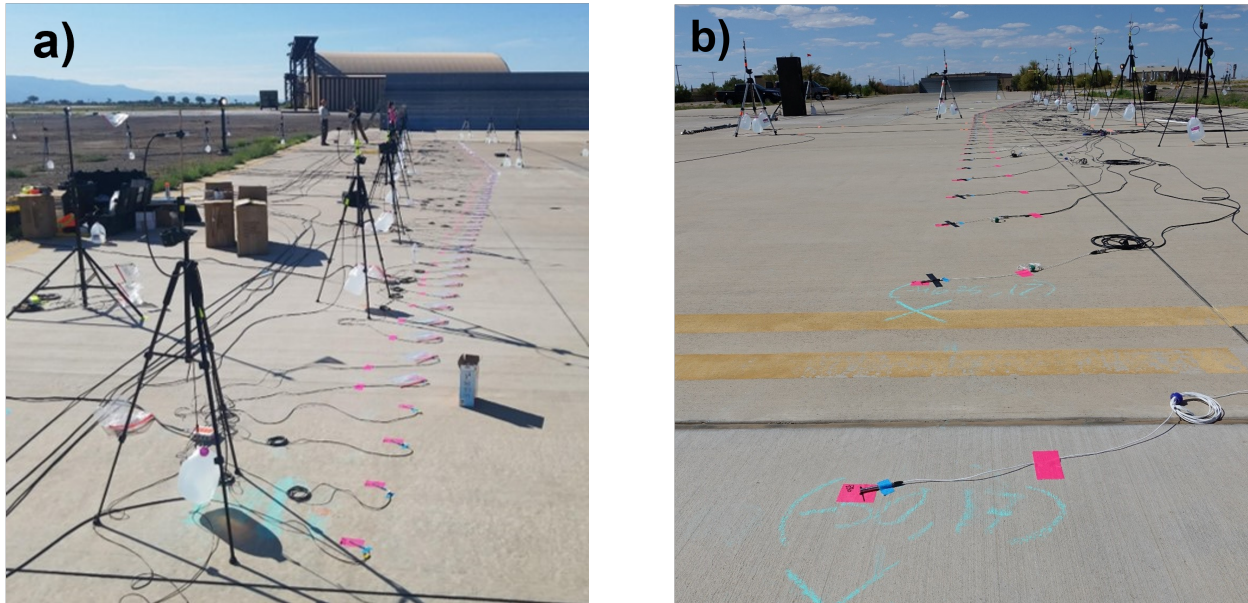


Figure 2.2 Images of microphones in the near-field ground array from two different directions: a) upstream towards the jet blast deflector, and b) downstream behind and away from the aircraft.

microphone locations show them mirrored on the right side for plotting convenience. Microphone positions were defined in both Cartesian coordinates and inlet angle, relative to a microphone array reference position (MARP) located 3.96 m (13 ft) downstream of the nozzle. Given a nominal exit diameter of 0.51 m (20 in), the MARP was located at 7.8 nozzle diameters. This same scaled MARP was used for prior aircraft analyses. The near-field ground array consisted of GRAS 1/4-inch 46BG and 46BD pressure and 46BE free-field microphones placed both upstream and downstream of the aircraft nozzle exit. They covered a range of inlet angles from 17.8° (upstream of the aircraft) to 165° (downstream of the aircraft). The microphones were oriented either pointed toward (46BE) or perpendicular (46BG and 46BD) to the MARP and taped to the ground. Figure 2.2 shows part of this array extending from upstream locations near the jet blast deflector (Fig. 2.2a) to downstream locations (Fig. 2.2b).

Moving upstream of the nozzle, the array linearly increased in y for a short distance, and then

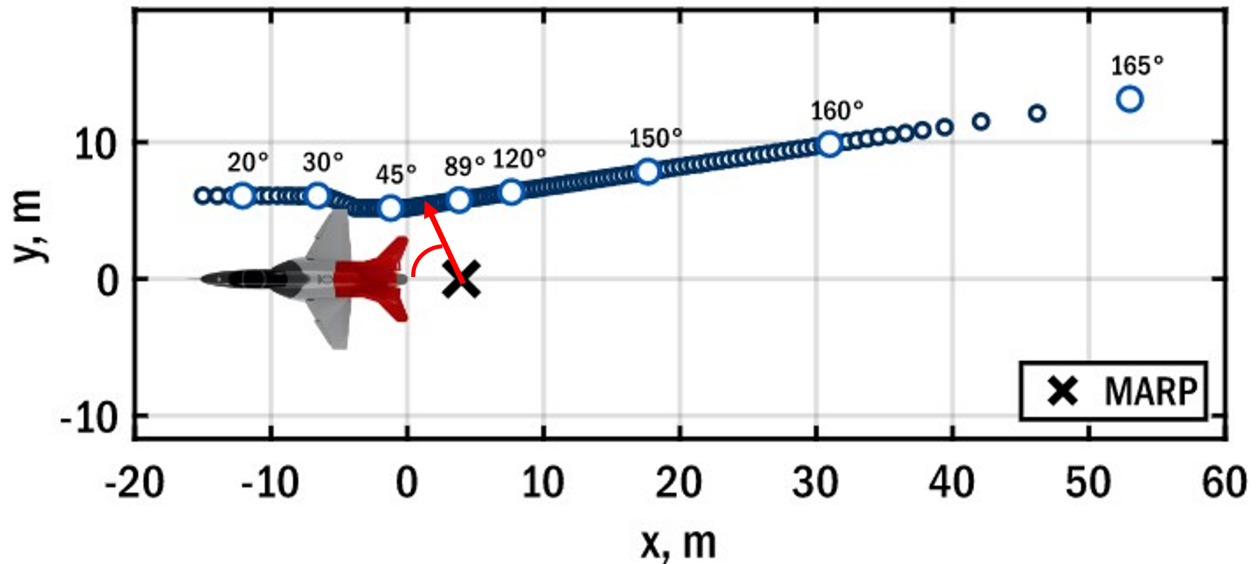


Figure 2.3 Locations of the near-field ground array microphones relative to the aircraft. The Microphone Array Reference Point (MARP) is indicated by the black x. White markers highlight specific angles along the array.

ran parallel to the jet axis as shown in Fig. 2.3. Downstream of the nozzle, the array ran parallel to the approximated shear layer, starting at approximately 60° (about 0.8 m aft of, or behind, the nozzle) and extending away from the aircraft. The spacing between microphones was determined based on predicted peak frequencies and prior experience, which resulted in smaller spacing towards the sideline of the jet and larger spacing aft of it, where lower frequencies were predicted to dominate. The near-field ground array extends farther upstream and downstream with smaller average spacing than was used in previous measurements of other high-performance aircraft [14, 15], which allow for finer spatial resolution and frequency bandwidth in analyses. Pressure waveforms were synchronously recorded using a 24-bit National Instruments PXIe system, with a sampling rate of 204.8 kHz for all 120 channels.

2.5 Encountering Non-Acoustic Sources of Noise

Even with optimal equipment and weather conditions, non-acoustic sources can affect the measurements taken. Some of these sources, specifically electromagnetic noise and preamplifier saturation, were seen to corrupt the data from some microphones in the near-field ground array. Some data validation processes were used to reduce the amount of contaminated data, although the effects could not be completely eradicated. For more details on the identification and eradication of these sources of noise, see the section on Data Validation in the paper by Leete *et al.* [23] Even with the effects of non-acoustic sources of noise, the data are valid enough for detailed analyses to be conducted across a large range of distances and frequencies.

Chapter 3

Results

3.1 Overview

This section presents the results of the similarity spectra and coherence analyses. The similarity spectra analysis characterizes jet noise sources based on peak level and peak frequency over a range of distances from the aircraft (Sec. 3.2). The coherence analysis characterizes jet noise sources based on the similarity of two signals at different locations over a range of frequencies (Sec. 3.3). Both analyses provide insight into the spatial and frequency behavior of the jet noise sources discussed in Sec. 1.3.

3.2 Applying the Similarity Spectra Analysis

The similarity spectra analysis is a useful starting point in identifying and characterizing jet noise sources. Using the formulas for $L_F(f)$, $L_L(f)$, and $L_B(f)$ (as described in Sec. 1.4), spectral models of the three main noise sources (FSN, LSN, and BSN) are generated and applied to the measured $L_p(f)$ spectra of the T-7A data. Spectral fits are only shown for two conditions: 88% N2 and afterburner. Spectral fits are shown at various inlet angles to portray the overall trends of

the turbulence structures. These conditions and angles are sufficient to examine key phenomena identified in this dataset.

3.2.1 At 88% N2

At angles upstream and to the side of the aircraft, the measured spectra at this intermediate engine condition exhibit broad, low-level peak behavior consistent with the characteristics of FSN. Tam *et al.*'s $L_F(f)$ [12] is fitted to these spectra to confirm their fine-scale behavior. At locations very far upstream, $L_F(f)$ is shown to match the low and middle frequencies of $L_p(f)$ while underestimating the levels of the high frequencies, as shown in Fig. 3.1a. Engine tones are present at this location and can be seen as a sharp spike at approximately 1500 Hz in Fig. 3.1a. As the inlet angle increases, the small discrepancies between measured and model spectra decrease until $L_F(f)$ fits the majority of the measured spectra. In Fig. 3.1b, however, the high-frequency slope of $L_p(f)$ decreases such that there is a larger gap between $L_p(f)$ and $L_F(f)$. The disagreements seen at high frequencies at these upstream locations are likely caused by the presence of other engine-related noise sources besides FSN. With increasing inlet angle, the peak frequency of $L_F(f)$ is found to decrease while the peak level tends to increase until approximately 118° , after $L_L(f)$ is included, at which point the contribution of $L_F(f)$ is no longer significant. These $L_F(f)$ trends match those found by Vaughn *et al.* [24] in their study on an unheated, Mach 1.8 laboratory-scale jet at both near- and mid-field locations. $L_L(f)$ is first included at 79° , although it could be argued that only $L_F(f)$ needs to be used to account for the majority of the spectrum until approximately 89° . In this analysis, however, it is determined that $L_L(f)$ should be included at that location to match and smooth out the trends of the overall sound pressure level. Figure 3.1c shows how both $L_F(f)$ and $L_L(f)$ are used to fit the measured spectrum.

As seen at 89° , the measured spectra at the sideline locations exhibit behaviors consistent with the characteristics of both FSN and LSN. At lower and higher frequencies, the slopes are shallow

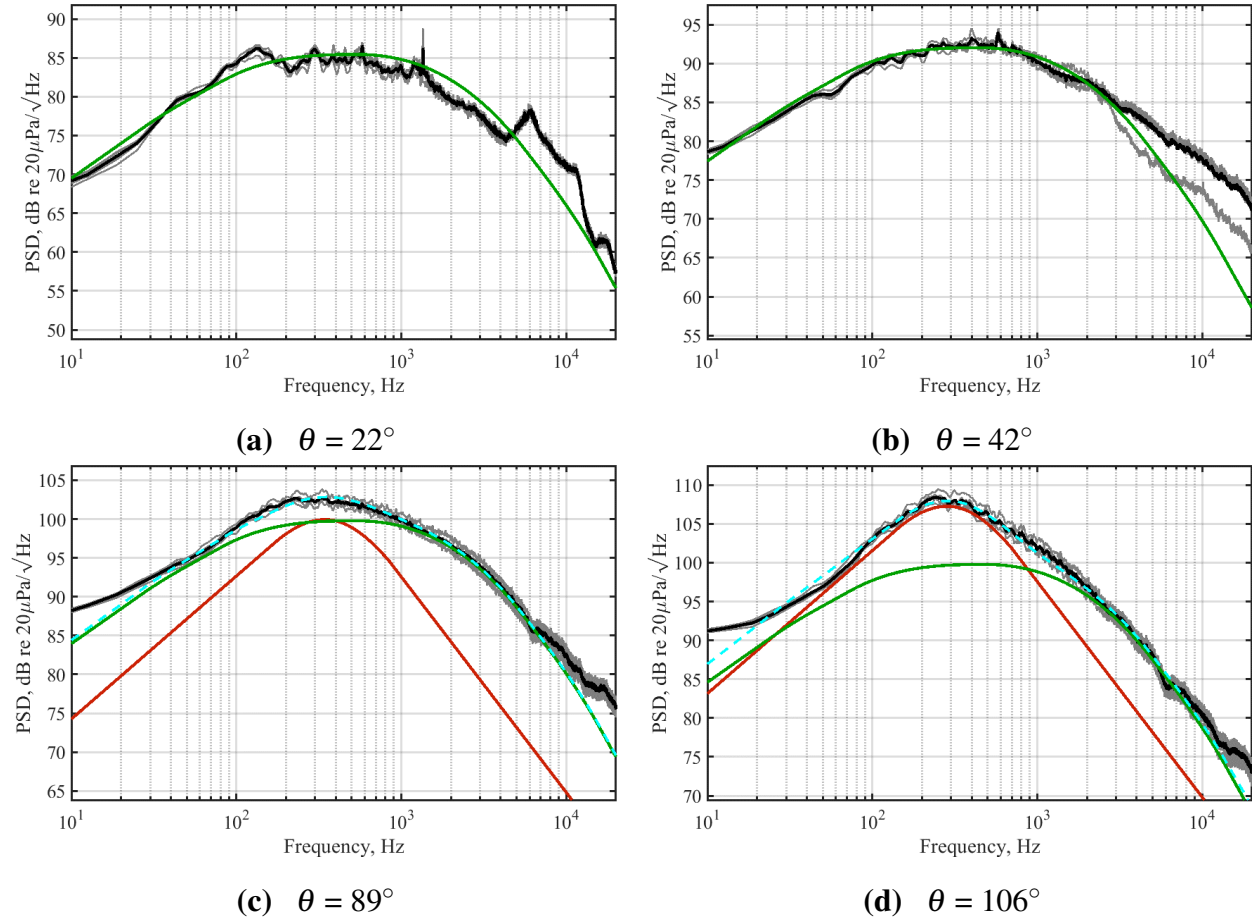


Figure 3.1 Similarity spectra fits for 88% N2 at (a) 22° , (b) 42° , (c) 89° , and (d) 106° . The gray curves indicate the measured spectra $L_p(f)$ of individual runs and the black curve is their average. The green curve is the fine-scale similarity spectrum $L_F(f)$, the red curve is the large-scale similarity spectrum $L_L(f)$, and the cyan dashed curve is the sum $L_T(f)$ of the two models.

and broad, which match the FSN characteristics, whereas the peaks of the measured spectra are sharper than can be accounted for with $L_F(f)$. $L_L(f)$, which exhibits this peak behavior, is therefore essential to capturing the characteristics of FSN and LSN. Figure 3.1d shows these behaviors more clearly than is observed at 89° . The very low and high frequencies have shallower slopes than what Tam *et al.*'s models [12] predict, but the overall fit matches $L_p(f)$ extremely well.

As the inlet angle continues to increase, the characteristics of LSN become a more dominant part

of the measured spectra until only $L_L(f)$ is necessary to capture those characteristics. This transition occurs aft of 124° . Figure 3.2a shows that there is very good agreement between $L_p(f)$ and $L_L(f)$ immediately downstream of 124° . The lower frequencies of the measured spectra have a steeper slope than $L_L(f)$ predicts, but since $L_L(f)$ very closely matches the levels at the other frequencies, they do not affect the overall fit. Farther downstream, $L_L(f)$ continues to agree with the high-frequency slopes of the measured spectra, as is evident in Fig. 3.2b. However, the low-frequency slope of $L_p(f)$ steepens to lower levels than are predicted by $L_L(f)$, and this trend continues from 128° to approximately 160° . The cause of these steep slopes is currently unknown. Another phenomenon to note is the presence of multiple peaks in the measured spectra. They begin to appear around 128° (see Fig. 3.2a) and persist at varying levels, frequencies, and number of distinct peaks until approximately 155° . These peaks are indicative of a “spatiospectral” lobing effect seen by Leete *et al.* [23] and observed in previous full-scale studies [8, 14–16] of high-performance aircraft, but their cause has yet to be definitively determined. In examining the overall trends of the peak frequency and level of $L_L(f)$ with increasing inlet angle, the peak frequency decreases while the peak level increases until approximately 134° , at which point the peak level begins to decrease. These trends were also observed by Vaughn *et al.* [24] and they continue to the end of the array.

Near the end of the array, hydrodynamic effects are likely evident in the variability of the levels between each run and in the shapes of the measured spectra. In Fig. 3.2c, the difference in level between each run is visible, but the shapes are still recognizable as those resulting from LSN, and thus $L_L(f)$ is applied. As the measured spectra near the very end of the array are examined, their spectral shapes become much less defined. While it is noticeable that most of the runs exhibit behavior somewhat typical of LSN, the peak becomes too broad for $L_L(f)$ to completely capture, as is shown in Fig. 3.2d. With the addition of the two $L_p(f)$ whose shapes show very little resemblance to those of the other runs, it is nearly impossible to conclusively identify any LSN characteristics. Figure 3.2d shows the result of this analysis in applying $L_L(f)$ to $L_p(f)$ at the end of the array,

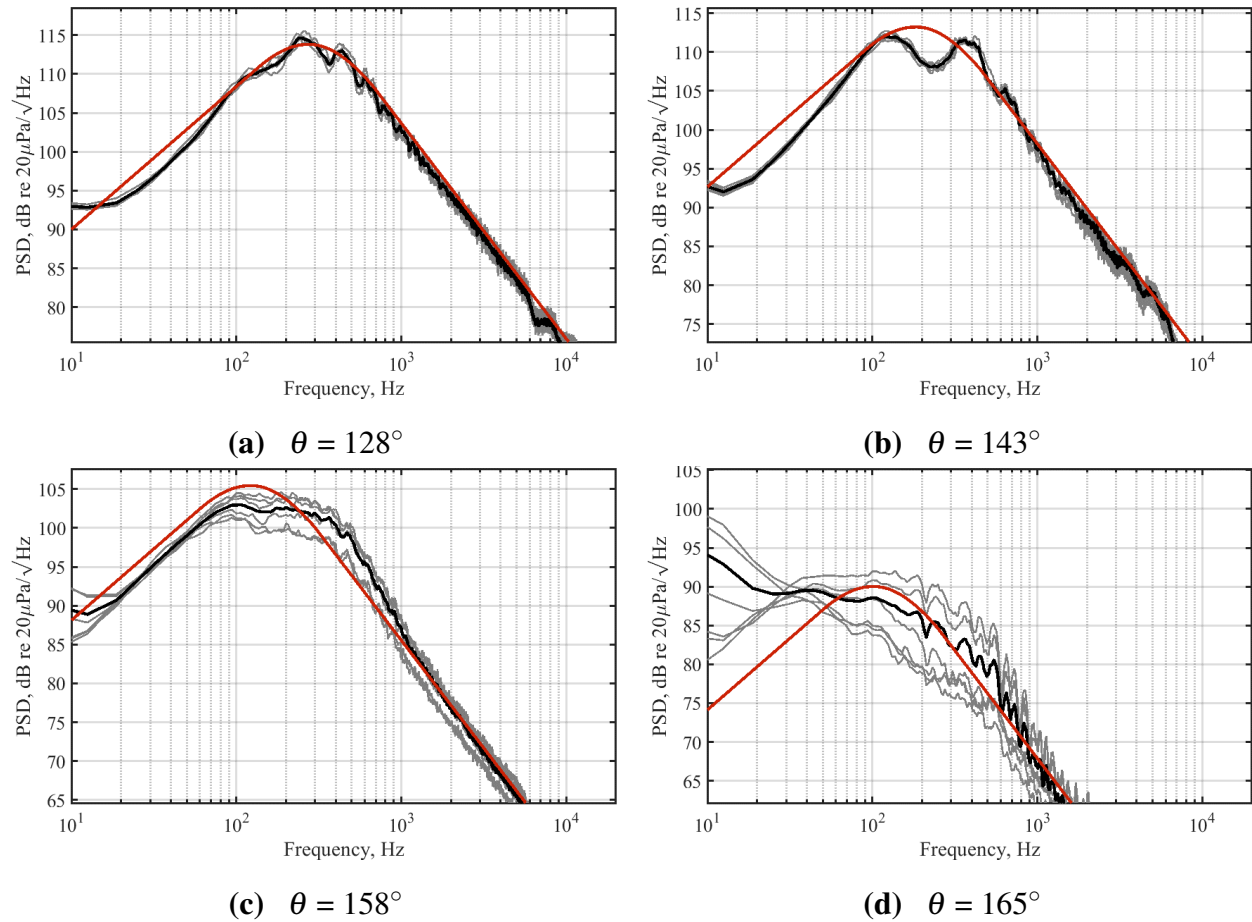


Figure 3.2 Similarity spectra fits for 88% N2 at (a) 128° , (b) 143° , (c) 158° , and (d) 165° . The gray curves indicate the measured spectra $L_p(f)$ of individual runs and the black curve is their average. The red curve is the large-scale similarity spectrum $L_L(f)$.

but because it is difficult to find a strong resemblance to the $L_L(f)$ shape using the average $L_p(f)$, it is not firmly proposed that this is the most accurate application of this analysis at this location. Whether the cause of such a lack of a distinct spectral shape is solely due to hydrodynamic effects or if there are other factors involved is not currently known.

3.2.2 At Afterburner

At higher engine conditions such as afterburner (AB), spectral behavior typical of BSN characteristics is expected to appear at upstream and sideline angles and is, in fact, observed in this dataset. Figure 3.3a shows the narrow and sharp peak representative of BSN behavior as well as the broad peak and shallower slopes consistent with FSN, both of which can be represented with $L_B(f)$ and $L_F(f)$, respectively. These models, while matching the general trends and shape of the BSN and FSN characteristics, do not account for the various bumps and nulls seen across the whole spectrum. For the low frequencies especially, $L_p(f)$ shows a shallower slope than $L_F(f)$ predicts. As inlet angle increases, it is found that the peak level of $L_F(f)$ steadily increases, whereas the peak frequency increases until approximately 52° , at which point it begins to decrease. $L_F(f)$ must still be applied when BSN is present to match the broad peak not accounted for by $L_B(f)$, but the slopes of $L_p(f)$ are shallower than $L_F(f)$ predicts and are thus underestimated, as seen in Fig. 3.3b.

Similar trends are also identified in $L_B(f)$ with increasing angle. The peak frequency and peak level of $L_B(f)$ increase until approximately 60° , at which point the peak level begins to decrease. The width of $L_B(f)$ remains relatively constant with increasing angle until 39° , at which point it narrows until it reaches 62° , where it begins to broaden once more. The trends identified in Nielsen *et al.* [15], Tam *et al.* [16], and Vaughn *et al.* [11] agree with those identified in the behavior of $L_B(f)$ in this analysis. Beginning at approximately 73° , however, the width of the peak of $L_p(f)$ becomes too wide for $L_B(f)$ to capture by itself, and the peak appears to exhibit some behaviors more consistent with LSN. Thus, all three predictive models are used (see Fig. 3.3c) to fit the measured spectra as accurately as possible. While no previous research has used both similarity spectra and a BSN model on the same spectrum, all three models are needed to identify the characteristics of both the mixing noise and the BSN present at this location.

$L_F(f)$, $L_L(f)$, and $L_B(f)$ are used to match the shape of $L_p(f)$ until approximately 89° , at which point only $L_F(f)$ and $L_L(f)$ are needed. In Fig. 3.3d, $L_L(f)$ captures the sharper peak while $L_F(f)$

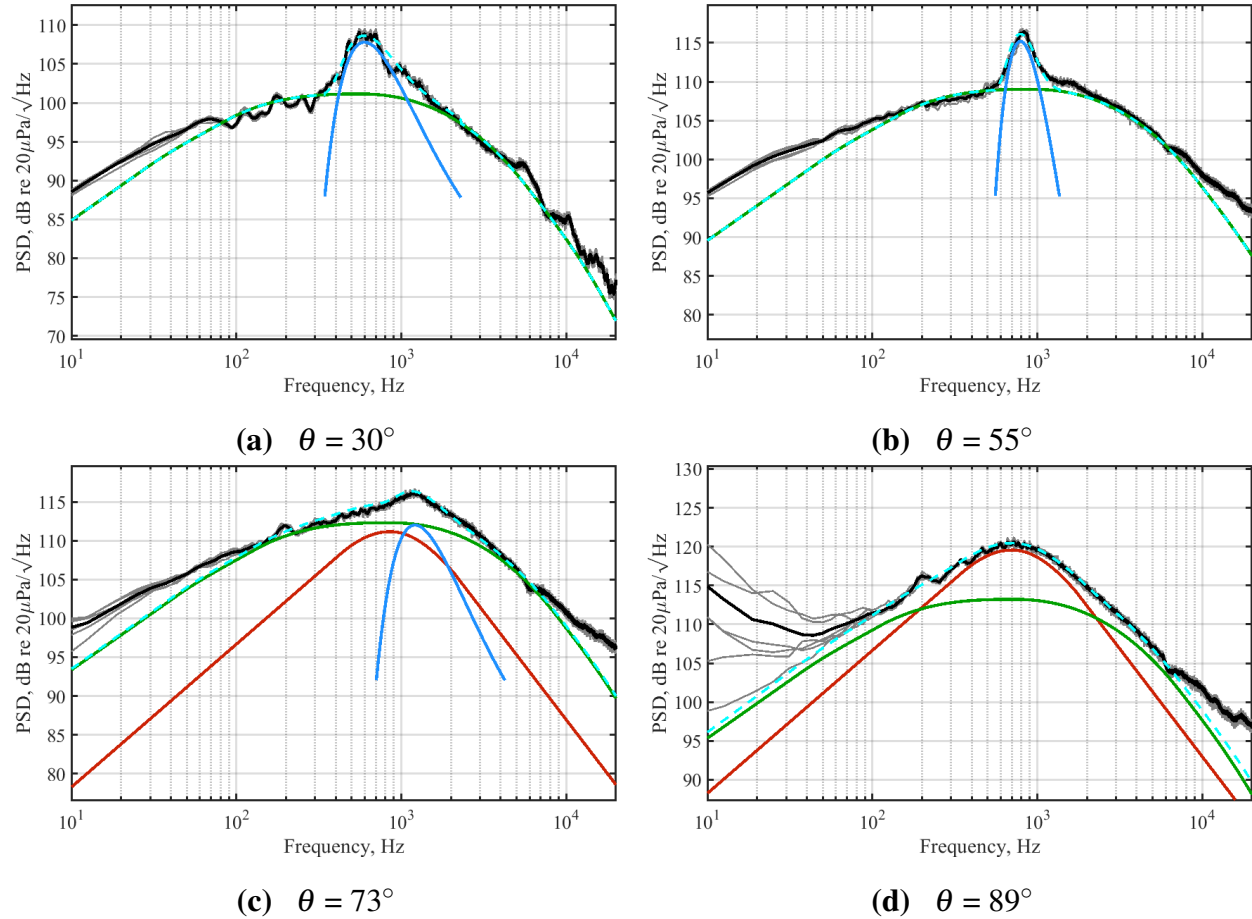


Figure 3.3 Similarity spectra fits for afterburner at (a) 30° , (b) 55° , (c) 73° , and (d) 89° . The gray curves indicate the measured spectra $L_p(f)$ of individual runs and the black curve is their average. The green curve is the fine-scale similarity spectrum $L_F(f)$, the red curve is the large-scale similarity spectrum $L_L(f)$, the blue curve is the BSN spectral model $L_B(f)$, and the dashed cyan curve is the sum $L_T(f)$ of any two or three of these models.

captures the shallower slopes. The $L_p(f)$ at low frequencies exhibit characteristics of microphone preamplifier saturation [23, 25], which can occur because of high-voltage, shock-like transients for higher-sensitivity microphones, and accounts for their atypical spectral behavior at those frequencies. At very high frequencies, however, a different source for the shallower slope is identified. Leete *et al.* [23] determined that, for AB conditions, the skewness of the pressure derivative (also known as derivative skewness) reached a value of 3 at approximately 3 m downstream of the nozzle. As

significant shock-like content present in the acoustic pressure waveforms (which appears in the form of shallower slopes at high frequencies) tends to occur at derivative skewness values above 3 [26, 27], the shallower slope seen at the high frequencies in Fig. 3.3d is due to the presence of shocks in the acoustic field. Schlinker *et al.* [28] also noticed a 5-7 dB/decade shallower slope at high frequencies that they attributed to the same phenomenon. These effects are evident in the measured spectra through the end of the array.

From angles 89° through 92° , only $L_F(f)$ and $L_L(f)$ are applied to the measured spectra. Downstream of those angles, the shallower high-frequency slope of the measured spectra is most likely due to nonlinear propagation effects rather than FSN. $L_L(f)$ is therefore the only model applied downstream of 92° , as shown in Fig. 3.4a. There are also underestimations at low frequencies due to shallow slopes, but the cause of this effect is unknown. Trends in the peak frequency and peak level of $L_L(f)$ are observed to be similar to those at the intermediate conditions. As inlet angle increases, the peak frequency decreases while the peak level increases until approximately 130° , at which point it begins to decrease.

Another phenomenon to note is the presence of multiple maxima and minima in the peak-frequency region of the measured spectra. These peaks are indicative of a “spatiospectral” lobing effect seen by Leete *et al.* [23] and observed in previous full-scale studies [8, 14–16] of high-performance aircraft, but their cause has yet to be definitively determined. This phenomenon is also observed at 88% N2 (see Sec. 3.2.1) Farther downstream, the multiple peaks detected evolve into two distinct peaks with a large null between them, as seen in Fig. 3.4b. The high-frequency slope still exhibits the shallow slope due to the presence of shocks in the acoustic field, but the low-frequency slope steepens drastically until the predicted low-frequency slope of $L_L(f)$ overestimates that of $L_p(f)$. This steep slope is observed in the measured spectra until approximately 154° .

Near the end of the array, the effects of hydrodynamic factors are once again identified in the differing levels between runs. Figure 3.4c, which shows those effects, also shows an interesting

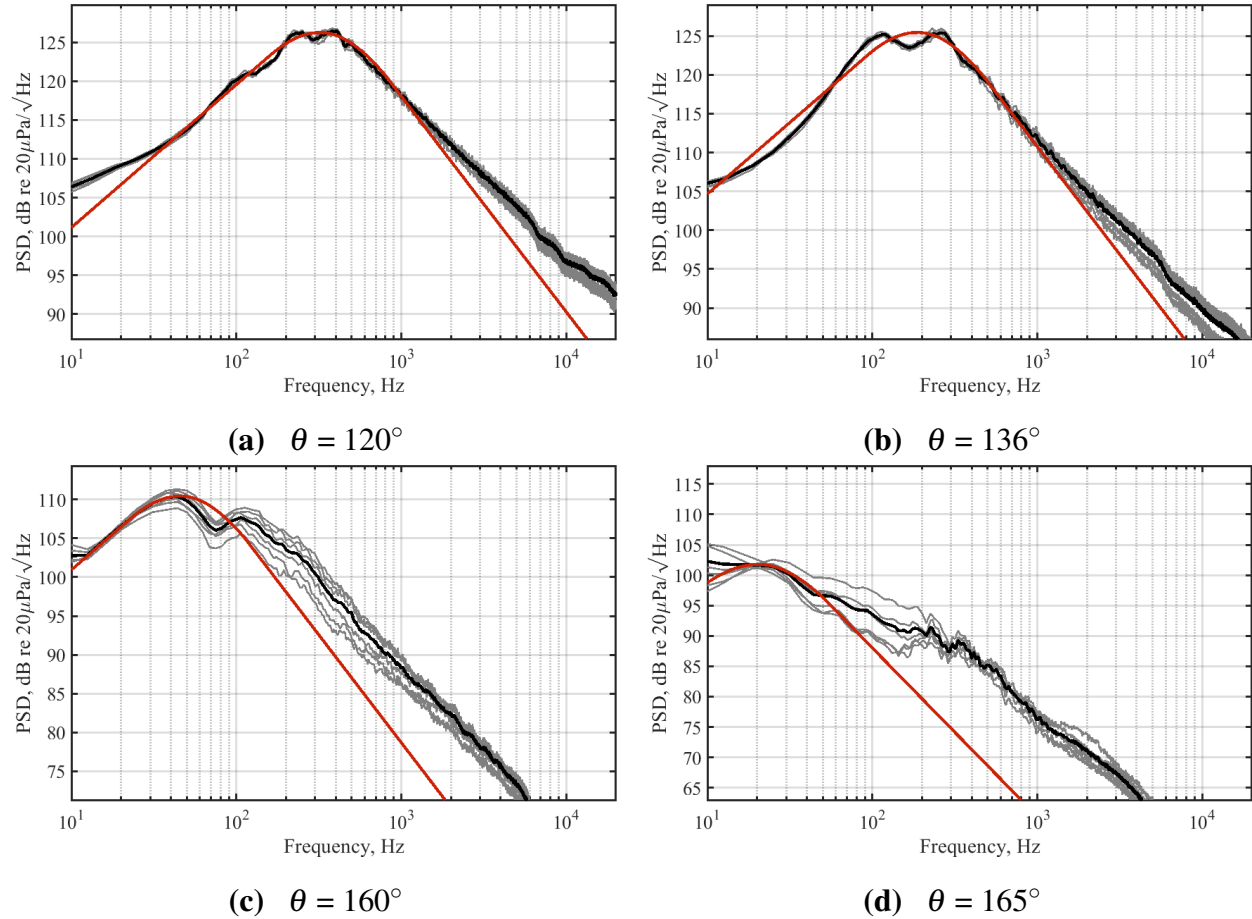


Figure 3.4 Similarity spectra fits for afterburner at (a) 120° , (b) 136° , (c) 160° , and (d) 165° . The gray curves indicate the measured spectra $L_p(f)$ of individual runs and the black curve is their average. The red curve is the large-scale similarity spectrum $L_L(f)$.

spectral behavior not seen at the intermediate conditions. A null generates a second peak that shifts the high-frequency slope to frequencies higher than $L_L(f)$ can predict, assuming the first peak in $L_p(f)$ is a result of LSN. The two peaks shown in Fig. 3.4c persist through the end of the array. This introduces an interesting dilemma in how to apply $L_L(f)$ to the end of this array because of the uncertainty of where on the frequency domain the LSN has the greatest effect. In following the trend of the peak frequency decreasing in value with increasing inlet angle, as well as following the expected predictions of low-frequency noise dominating in the downstream region, $L_L(f)$ is applied to the first peak in this analysis. Whether this is where $L_L(f)$ should be applied or not is

still uncertain. Tam and Parrish [8] identified similar behavior in their study of data from another installed engine, but a confirmed source of the second peak remains to be determined. At the end of the array (165° , see Fig. 3.4d), the shapes of $L_p(f)$ are still most likely affected by hydrodynamics and become less distinct, as is the case at the 88% N2 condition. There is a possible low-frequency peak to which $L_L(f)$ has been fit, but the lack of a defined spectral shape makes this application less certain. A $L_L(f)$ spectral peak in the 200-300 Hz region could just as easily have been chosen.

3.3 Applying the Coherence Analysis

The coherence analysis provides additional insight into the behavior of FSN, LSN, and BSN that the similarity spectra analysis does not capture. Using the formula for coherence as described in Sec. 1.5, coherence plots are generated over a frequency range of 2 Hz to 998 Hz. A few frequencies are selected to highlight various trends and phenomena seen at the 88% N2 and AB engine conditions.

3.3.1 At 88% N2

The coherence plots produced for the 88% N2 engine condition exhibit similar trends over distance and frequency to what is expected in a coherence analysis. As frequency increases, the coherence levels decrease across the whole microphone array (Fig. 3.5). This is consistent with what has been identified in previous research [19–21].

At sideline locations, FSN is the dominant source of noise. Because FSN mostly consists of random and incoherent signals, regions where FSN dominates are expected to show low coherence levels. As Fig. 3.5a and Fig. 3.5b demonstrate, sideline locations between 50° and 90° show very low levels of coherence, indicating that this region is dominated by FSN. As frequency increases, the coherence levels are seen to decrease at locations upstream of 50° until they appear to have the same range of levels as the sideline region. Because FSN is the dominant source of noise at

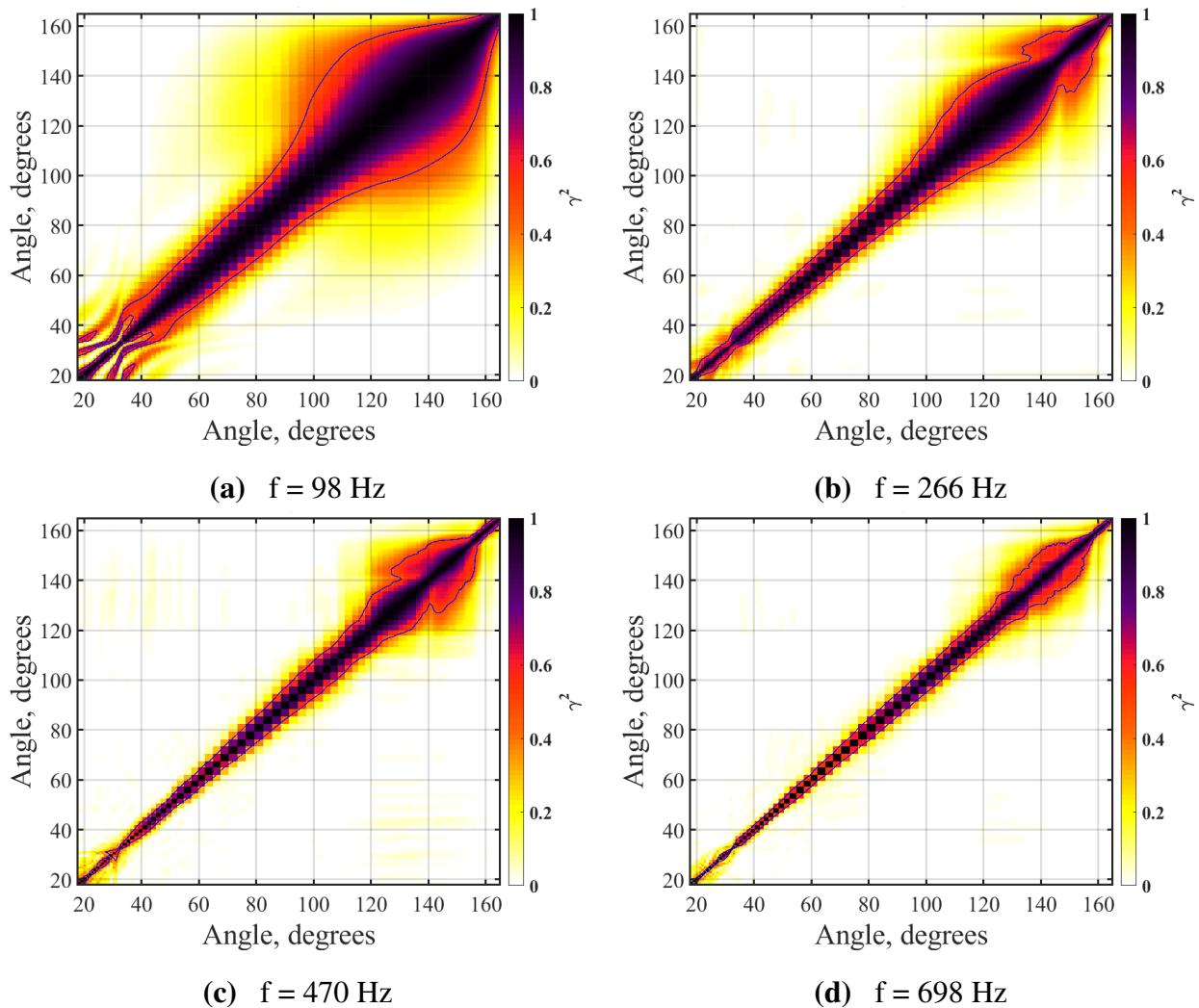


Figure 3.5 Coherence maps for 88% N2 at (a) 98 Hz, (b) 266 Hz, (c) 470 Hz, and (d) 698 Hz. A higher coherence value indicates a greater similarity between the signals compared at two different locations.

upstream locations for this engine condition, it follows that the levels are low in this region. An interesting fingering effect is noted at the lowest frequencies in this upstream region, but no cause has been identified.

At downstream locations, LSN is the dominant noise source. Because LSN is generally more coherent than FSN, it is expected that regions where LSN dominates will have higher levels of coherence. As Fig. 3.5a and Fig. 3.5b show, larger regions of high coherence are seen at downstream

locations. This indicates that LSN is the dominant source of noise aft of approximately 90° .

When looking at the spectra at the 88% N2 engine condition, there is no evidence of sharp peaks at upstream locations to suggest that BSN is generated at this engine power. By observing the coherence plots, however, there is some evidence that BSN might be present. In Fig. 3.5c, low levels of coherence are identified as pale yellow bands when comparing the 20° - 70° and 120° - 160° regions between 300 Hz and 600 Hz. Bands like these are typically expected to appear at high engine conditions when BSN is present. Because these bands appear at 88% N2, they are indicative of the presence of BSN, and therefore shock cells, in the potential core. The low levels that these bands exhibit imply that the shock cells might only be just beginning to form (and therefore 88% N2 is transonic) and haven't developed into the clear shock cells seen at higher engine conditions (which are supersonic).

3.3.2 At Afterburner

The coherence plots produced for the afterburner (AB) engine condition exhibit similar trends over distance and frequency to what is expected in a coherence analysis. As frequency increases, the coherence levels decrease across the whole microphone array. The coherence levels for AB are also lower at this engine condition than are observed at 88% N2 (compare Fig. 3.6 to Fig. 3.5). This is consistent with what has been identified in previous research [19–21]. It is noted that the large plus sign in Fig. 3.6a is a result of saturation, but it has a negligible effect on the results of this analysis.

At sideline locations, FSN is again observed to be the dominant source of noise due to the low levels of coherence seen between 60° and 80° . Upstream of 60° , however, there appear to be higher levels of coherence than is observed in this region at 88% N2 (see Fig. 3.6a and Fig. 3.6b). This is most likely due to the presence of BSN, which radiates upstream and is co-dominant with FSN in that region. Because BSN is more coherent than FSN, it follows that the coherence levels are higher at these upstream locations. The bands of coherence observed at the 88% N2 condition between

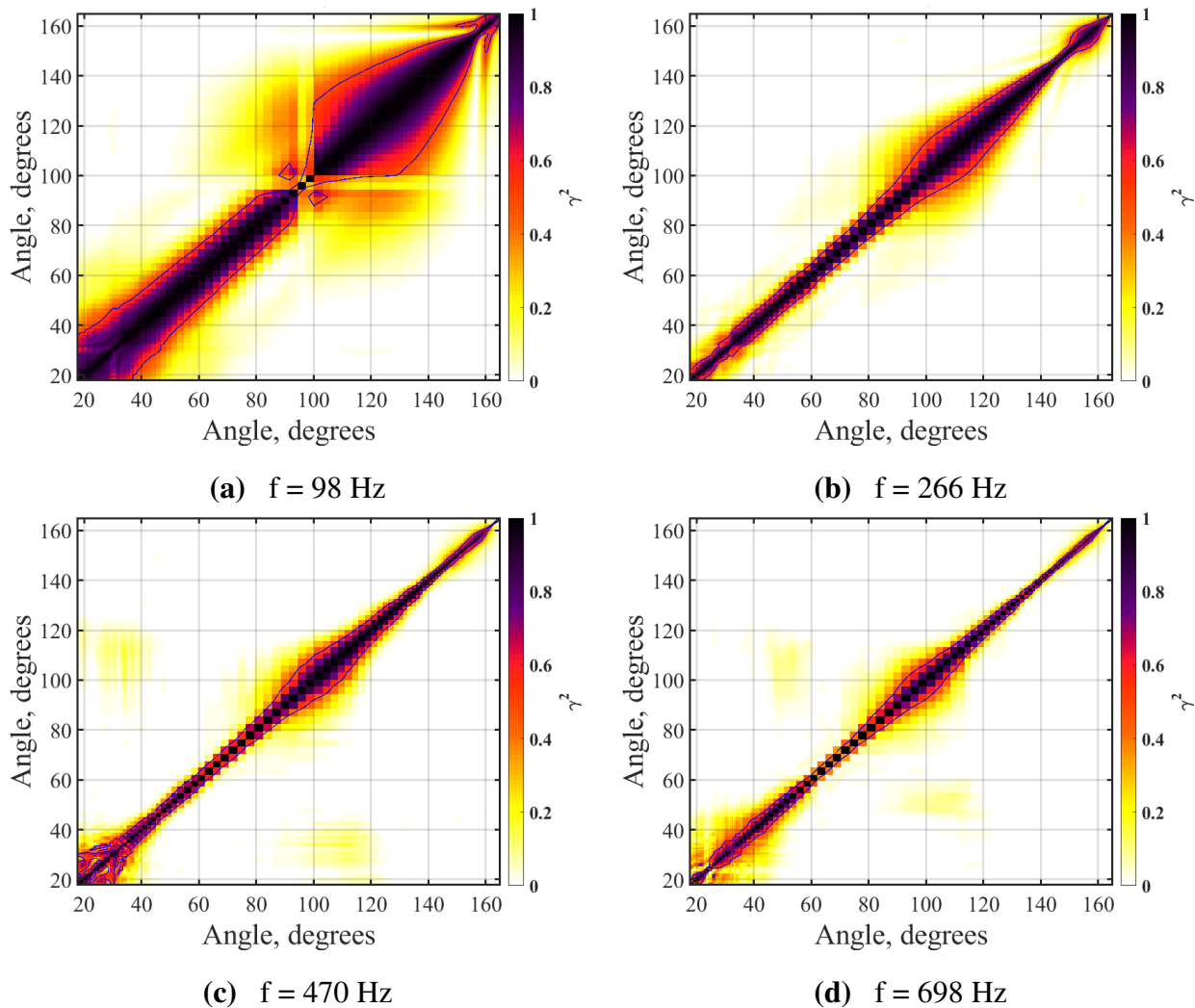


Figure 3.6 Coherence maps for afterburner at (a) 98 Hz, (b) 266 Hz, (c) 470 Hz, and (d) 698 Hz. A higher coherence value indicates a greater similarity between the signals compared at two different locations. The large plus sign that appears in (a) is due to saturation effects that occur at low frequencies. It has no noticeable impact on the analysis.

upstream and downstream locations (Fig. 3.5c) are seen at AB as well, indicating once again that BSN is present. These bands, however, show a higher level of coherence, which is expected because BSN is much more dominant at AB than at lower engine conditions. They are also much more concentrated than the bands seen at 88% N2 and appear in the 350-800 Hz range, as observed in Fig. 3.6c and Fig. 3.6d. This is most likely because the shock cells in the potential core are much more

defined, which would make the radiation properties of BSN much more defined and concentrated. The fact that these bands exist at engine powers that generate BSN indicates a possible connection between BSN and Mach wave radiation. While a definitive cause has not been identified, Swift *et al.* [20] proposes that these bands could have two possible sources: 1) BSN radiates not only upstream but also downstream, or 2) BSN is imprinted on the Mach waves that carry those signals downstream.

At downstream locations aft of 80° , there are again larger regions of higher coherence than is observed at upstream and sideline locations (most easily identified in Fig. 3.6a and Fig. 3.6b). This behavior is consistent with LSN radiation properties since LSN is known to be the dominant noise source at downstream locations and is known to have higher coherence than FSN. Because of the higher engine power, however, the coherence levels in this region are notably lower than is seen in this region at 88% N2.

3.4 Decomposing the Spatiospectral Lobes

When observing the sound pressure levels over varying frequencies and distances, large peak regions separated by small regions of lower levels can be identified. These peak regions are known as spatiospectral lobes. This phenomenon is widely studied using different methods to further understand the characteristics and behavior of the lobes [19, 20, 29, 30]. While no definitive cause has been identified, spatiospectral lobes are observed to be a key feature of full-scale analyses with little to no evidence of their existence in laboratory-scale measurements [30]. The similarity spectra and coherence analyses each highlight different features and characteristics of these lobes in the T-7A data. Only figures for 88% N2 and afterburner are shown.

The measured sound pressure levels in the direction of maximum radiation, as seen in Fig. 3.7a, have multiple peaks. These peaks, observed at the same location, appear at different frequencies. By

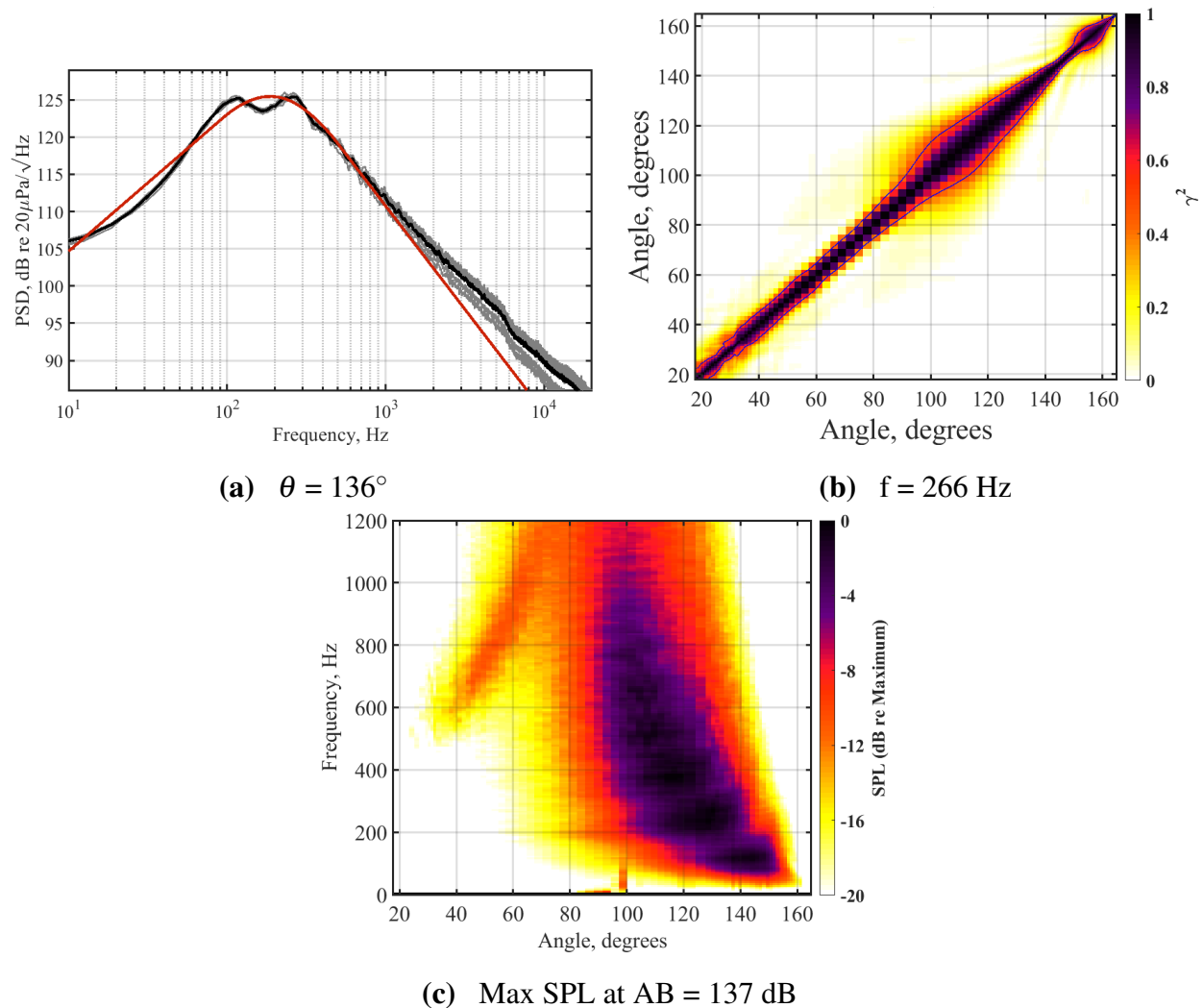


Figure 3.7 The two analyses discussed provide insight into the spatio-spectral lobe phenomenon. The spectrum at 136° in (a) and the coherence map at 266 Hz in (b) show double peaks that appear in the spatio-spectral map in (c). The spatio-spectral map portrays the sound levels over distance and frequency, and the spatio-spectral lobe phenomenon appears clearly here. The levels on the colorbar are defined with respect to the maximum sound level at afterburner. The small increase in level at very low frequencies at approximately 100° is due to saturation.

looking at a spatio-spectral map of the measured levels in Fig. 3.7c, the same behavior can be seen in the multiple peak regions over different frequencies at the same location. Because the similarity spectra do not have multiple peaks, they therefore do not show evidence of spatio-spectral lobes.

Since they were generated using laboratory-scale data [12], it can be inferred that laboratory-scale measurements in general do not generate these lobes.

The coherence analysis can similarly be used to identify the behavior of spatio-spectral lobes. While it does not identify any probable cause of the spatio-spectral lobe phenomenon, it does provide further insight into some of its characteristics. The coherence map in Fig. 3.7b shows two peak regions between 90° - 130° and between 150° - 160° in the coherence levels at 266 Hz. These peak regions correspond to the spatio-spectral lobes seen at the same angles and frequencies in Fig. 3.7c. Because of this, some characteristics of the lobes are identified. First, each lobe is self-coherent. Second, the lobes are not coherent with each other. This behavior, also seen in Harker *et al.* [19] and Swift *et al.* [20], implies that the spatio-spectral lobes are generated by different, distinct sources. The regions of lower levels between the lobes on the spatio-spectral maps are therefore caused by their competing coherence. Identifying these characteristics of the lobe behavior helps eliminate the theory that the lobes are all generated by the same source. Were that to be the case, even if the noise from this single source was diffracted or reflected such that the lobes appear as they do, there would be evidence of coherence between the angles where the lobes appear. As this is not seen in Fig. 3.7b, it can be concluded that the lobes are generated by different and competing sources.

3.5 Conclusion

Despite being developed from far-field, laboratory-scale data, Tam *et al.*'s similarity spectra [12] and Kuo *et al.*'s BSN model [7] appear to generally identify the behaviors of fine-scale noise (FSN), large-scale noise (LSN), and broadband shock-associated noise (BSN) in the measured spectra of a near-field ground array at 88% N2 and afterburner (AB) conditions. Performing this analysis helps confirm that the FSN dominates the upstream and sideline regions of the aircraft, the LSN dominates downstream, and the BSN co-dominates with FSN at higher engine powers. A transition

region consisting of FSN and LSN occurs just downstream of the nozzle for both engine conditions, with an additional transition region consisting of BSN and FSN and LSN occurring at AB. The peak frequency and peak level of the fine-scale similarity spectrum $L_F(f)$ and the large-scale similarity spectrum $L_L(f)$ show somewhat similar trends between the intermediate and AB conditions across the entire array. For $L_F(f)$, the peak frequency at 88% N2 decreases while at AB it increases and then decreases with increasing inlet angle. The peak level of $L_F(f)$ increases then decreases with increasing angle for both conditions, but the point at which it decreases differs for each condition. For $L_L(f)$, the peak frequency decreases and the peak level increases and then decreases for both engine powers. Once again, however, the angle at which the peak level of $L_L(f)$ begins to decrease differs for each condition. The trends in the characteristics of the BSN spectral model ($L_B(f)$) match what was found by Neilsen *et al.* [15] at high engine powers. As inlet angle increases, the peak frequency increases and the peak level increases and then decreases. The width of $L_B(f)$ remains relatively constant until 39° , at which point it decreases until it reaches an angle of 62° where it starts to increase.

The application of the similarity spectra to the measured spectra is successful, but there are two phenomena identified in this analysis that cannot be accounted for by the similarity spectra. The first one is the presence of double peaks in the measured spectra at downstream locations for both the 88% N2 and AB engine condition. While no potential causes for this behavior have been identified or discussed in this paper, the analysis of this dataset contributes to the number of other studies [8, 14–16] that have also seen double peaks in their spectra, thereby providing additional data for future studies on spatiospectral lobes. The second phenomenon noted in this study is the deterioration of the spectral shapes near the end of the array for both engine conditions. Because this study placed microphones farther downstream than other full-scale tests have done before, the lack of distinct, single-peaked spectra is a behavior not observed to date. Whether hydrodynamic factors, the lack of dominant LSN, or a different source of noise are the cause of this phenomenon

is still unknown and requires further study.

The spatial and frequency trends in coherence match what is observed in previous studies [19–21]. For both 88% N2 and AB, the coherence levels decrease with increasing frequencies, and the levels at AB are lower than those at 88% N2. Low levels of coherence are observed at sideline locations and large regions of high coherence are observed at downstream locations, consistent with the coherence properties of FSN and LSN, respectively. BSN causes the levels at upstream locations to increase at AB. Low-level bands of coherence between upstream and downstream locations are observed at both engine conditions, indicating the presence of BSN and shock cells. Because the coherence levels of these bands at 88% N2 are lower than those at AB, this implies that the shock cells have not completely formed yet and BSN is not as dominant as it is at AB. Two possible explanations for observing the presence of BSN at downstream locations are: 1) BSN radiates in both upstream and downstream directions, and 2) the signals containing BSN are imprinted on the Mach waves that radiate downstream, so a copy of the BSN signals is observed downstream.

Properties of the spatio-spectral lobes are observed in comparison to both analyses discussed in this thesis. The double peak phenomenon seen in the measured spectra correspond to these lobes, yet the double peaks are not seen in laboratory-scale measurements. This implies that the spatio-spectral lobes only appear and influence the sound levels in full-scale environments. The multiple peaks seen in the coherence analysis indicate that the spatio-spectral lobes are self-coherent but not mutually coherent. It can therefore be concluded that the lobes are not created by a single source, but rather each lobe is created by a different source and the resulting noise competes with the other lobes, creating the regions of lower coherence observed in the coherence maps and the regions on lower sound levels in the spatio-spectral maps.

These analyses of the three noise components and the coherence of the signals between microphones provide a useful starting point in characterizing the sources of jet noise for this dataset on an installed GE F404-103 engine. Future work involving coherence lengths, spatio-spectral

decompositions, and comparisons to far-field data will provide further insight into the applicability of the similarity spectra analysis on full-scale field tests of high-performance aircraft and the phenomenological behavior observed in this study.

Bibliography

- [1] J. Yong and D.-Y. Wang, “Impact of noise on hearing in the military,” *Military Medical Research* **2**, 6 (2015).
- [2] D. Casalino, F. Diozzi, R. Sannino, and A. Paonessa, “Aircraft noise reduction technologies: A bibliographic review,” *Aerospace Science and Technology* **12**, 1–17 (2008).
- [3] B. Greska, A. Krothapalli, J. M. Seiner, B. Jansen, and L. Ukeiley, “The effects of microjet injection on an F404 jet engine,” In *Collection of Technical Papers - 11th AIAA/CEAS Aeroacoustics Conference*, 11th AIAA/CEAS Aeroacoustics Conference **5**, 3051–3073 (2005).
- [4] J. M. Seiner, L. S. Ukeiley, and B. J. Jansen, “Aero-performance efficient noise reduction for the F404-400 engine,” In *11th AIAA/CEAS Aeroacoustics Conference*, 11th AIAA/CEAS Aeroacoustics Conference **5**, 3074–3086 (2005).
- [5] M. Samimy, K. B. M. Q. Zaman, and M. F. Reeder, “Effect of tabs on the flow and noise field of an axisymmetric jet,” *AIAA Journal* **31**, 609–619 (1993).
- [6] C. K. W. Tam, K. Viswanathan, K. K. Ahuja, and J. Panda, “The sources of jet noise: experimental evidence,” *Journal of fluid mechanics* **615**, 253–292 (2008).
- [7] C.-W. Kuo, D. K. McLaughlin, P. J. Morris, and K. Viswanathan, “Effects of Jet Temperature on Broadband Shock-Associated Noise,” *AIAA journal* **53**, 1515–1530 (2015).

-
- [8] C. K. W. Tam and S. A. Parrish, “Noise of high-performance aircraft at afterburner,” *Journal of sound and vibration* **352**, 103–128 (2015).
- [9] M. Ponton and J. Seiner, “The effects of nozzle exit lip thickness on plume resonance,” *Journal of Sound and Vibration* **154**, 531–549 (1992).
- [10] J. PANDA, “An experimental investigation of screech noise generation,” *Journal of Fluid Mechanics* **378**, 71–96 (1999).
- [11] A. B. Vaughn, T. B. Neilsen, K. L. Gee, A. T. Wall, J. Micah Downing, and M. M. James, “Broadband shock-associated noise from a high-performance military aircraft,” *The Journal of the Acoustical Society of America* **144**, EL242–EL247 (2018).
- [12] C. Tam, M. Golebiowski, and J. Seiner, “On the two components of turbulent mixing noise from supersonic jets,” In *Aeroacoustics Conference*, 2nd AIAA/CEAS Aeroacoustics Conference pp. 1–17 (American Institute of Aeronautics and Astronautics, 1996).
- [13] B. M. Harker, K. L. Gee, T. B. Neilsen, A. T. Wall, S. A. McInerny, and M. M. James, “On autocorrelation analysis of jet noise,” *The Journal of the Acoustical Society of America* **133**, EL458–EL464 (2013).
- [14] T. B. Neilsen, K. L. Gee, A. T. Wall, and M. M. James, “Similarity spectra analysis of high-performance jet aircraft noise,” *The Journal of the Acoustical Society of America* **133**, 2116–2125 (2013).
- [15] T. B. Neilsen, A. B. Vaughn, K. L. Gee, S. H. Swift, A. T. Wall, J. M. Downing, and M. M. James, “Three-Way Spectral Decompositions of High-Performance Military Aircraft Noise,” *AIAA journal* **57**, 3467–3479 (2019).

- [16] C. K. Tam, A. C. Aubert, J. T. Spyropoulos, and R. W. Powers, in *On the Dominant Noise Components of Tactical Aircraft: Laboratory to Full Scale, 23rd AIAA/CEAS Aeroacoustics Conference* (American Institute of Aeronautics and Astronautics, 2017).
- [17] T. B. Neilsen, K. L. Gee, B. M. Harker, and M. M. James, “Level-educed Wavepacket Representation of Noise Radiation from a High-Performance Military Aircraft,” In *54th AIAA Aerospace Sciences Meeting, 54th AIAA Aerospace Sciences Meeting* (American Institute of Aeronautics and Astronautics, 2016).
- [18] K. A. Epps, C. D. Merrill, A. B. Vaughn, K. M. Leete, K. L. Gee, and A. T. Wall, “Preliminary similarity spectra analysis of noise from a high-performance trainer aircraft,” In *Proceedings of Meetings on Acoustics*, Proceedings of Meetings on Acoustics 42 (Acoustical Society of America, 2020).
- [19] B. M. Harker, T. B. Neilsen, K. L. Gee, A. T. Wall, and M. M. James, “Spatiotemporal-Correlation Analysis of Jet Noise from a High-Performance Military Aircraft,” *AIAA journal* **54**, 1554–1566 (2016).
- [20] S. H. Swift, K. L. Gee, T. B. Neilsen, A. T. Wall, J. M. Downing, and M. M. James, in *Spatiotemporal-correlation analysis of jet noise from a round nozzle high-performance aircraft, 2018 AIAA/CEAS Aeroacoustics Conference* (American Institute of Aeronautics and Astronautics, 2018).
- [21] K. Leete, K. Gee, J. Liu, and A. Wall, in *Coherence Analysis of the Noise from a Simulated Highly-heated Laboratory-scale Jet* (2020), No. 8, pp. 3426–3435.
- [22] G.E.Aviation, “F404 Turbofan Engines,” <https://www.geaviation.com/sites/default/files/datasheet-F404-Family.pdf>, 2014, accessed: 24 April 2023.

- [23] K. M. Leete, A. B. Vaughn, M. S. Bassett, R. D. Rasband, D. J. Novakovich, K. L. Gee, S. C. Campbell, F. S. Mobley, and A. T. Wall, in *Jet Noise Measurements of an Installed GE F404 Engine, AIAA Scitech 2021 Forum* (American Institute of Aeronautics and Astronautics, 2021).
- [24] A. B. Vaughn, T. B. Neilsen, K. L. Gee, K. Okamoto, and M. Akamine, “Near-field spatial variation in similarity spectra decomposition of a Mach 1.8 laboratory-scale jet,” In *Proceedings of Meetings on Acoustics*, Proceedings of Meetings on Acoustics 29 (Acoustical Society of America, 2016).
- [25] T. Taylor, K. L. Gee, J. H. Giraud, S. D. Sommerfeldt, J. D. Blotter, and C. P. Wiederhold, “On the use of prepolarized microphone systems in rocket noise measurements,” In *Proceedings of Meetings on Acoustics*, Proceedings of Meetings on Acoustics 14 (2012).
- [26] B. O. Reichman, M. B. Muhlestein, K. L. Gee, T. B. Neilsen, and D. C. Thomas, “Evolution of the derivative skewness for nonlinearly propagating waves,” *The Journal of the Acoustical Society of America* **139**, 1390–1403 (2016).
- [27] K. L. Gee, P. B. Russavage, T. B. Neilsen, S. Hales Swift, and A. B. Vaughn, “Subjective rating of the jet noise crackle percept,” *The Journal of the Acoustical Society of America* **144**, EL40–EL45 (2018).
- [28] R. H. Schlinker, S. A. Liljenberg, D. R. Polak, K. A. Post, and C. T. Chipman, “Supersonic Jet Noise Source Characteristics and Propagation: Engine and Model Scale,” In *13th AIAA/CEAS Aeroacoustics Conference (28th AIAA Aeroacoustics Conference)*, 13th AIAA/CEAS Aeroacoustics Conference pp. 1–17 (American Institute of Aeronautics and Astronautics, 2007).
- [29] K. Leete, A. Wall, K. Gee, T. Neilsen, M. James, and J. Downing, in *Dependence of High-performance Military Aircraft Noise on Frequency and Engine Power, 2018 AIAA/CEAS Aeroacoustics Conference* (American Institute of Aeronautics and Astronautics, 2018).

-
- [30] A. T. Wall, K. L. Gee, T. B. Neilsen, S. A. McNerny, and M. M. James, in *Investigation of multi-lobed fighter jet noise sources using acoustical holography and partial field decomposition methods*, 21st AIAA/CEAS Aeroacoustics Conference (American Institute of Aeronautics and Astronautics, 2015).

Index

82% N2, 11

88% N2, 11, 16, 24

Afterburner, 8, 11, 20, 26

Broadband shock-associated noise, 3, 5, 7, 20,
26

Coherence, 6, 24

Fine-scale noise, 3, 4, 7, 16, 20, 24, 26

Large-scale noise, 3, 4, 7, 16, 20, 25, 28

Mach wave radiation, 28

Military Power, 11

Saturation, 14, 21, 26, 29

Similarity spectra, 4, 15

Spatiospectral lobes, 18, 22, 28

T-7A Red Hawk aircraft info, 8